EFFECTS OF HALO-NUCLEAR CORE SIZE ON GROUND-STATE PROPERTIES OF HALO NUCLEI

BY

THANDO TIMAX KHEDZI

EFFECTS OF HALO-NUCLEAR CORE SIZE ON GROUND-STATE PROPERTIES OF HALO NUCLEI

by

THANDO TIMAX KHEDZI

submitted in accordance with the requirements
for the degree of

MASTER OF SCIENCE

in the subject

PHYSICS

at the

UNIVERSITY OF SOUTH AFRICA

SUPERVISOR : PROFESSOR G. J. RAMPHO

JANUARY 2021

Declaration

Student : T. T Khedzi

Student No. : 5767 0781

I declare that **"EFFECTS OF HALO-NUCLEAR CORE SIZE ON GROUND-STATE PROPERTIES OF HALO NUCLEI"** is my own work and that all the sources that I have used or quoted have been indicated and acknowledged by means of complete references.

SIGNATURE DATE

Acknowledgments

I would like to thank Prof G. J. Rampho for his expert guidance, patience and inspiration throughout this research.

I would like to thank Dr B. Mukeru for his guidance and valuable discussions that shaped the direction of this work.

I thank my friend and fellow student, Mr. M. Ramantswana, for his encouragement and support during this research.

I thank my mother, Mrs. N. M. Khedzi, and my late father, E. Khedzi, for encouragement and support.

I thank my friend, N. Mphephu, for his wisdom.

I thank my brothers, A. Khedzi and C. Khedzi, for the encouragement.

I thank M. Sedibeng for the encouragement.

I also would like to thank the University of South Africa and the National Research Foundation for financial support.

Summary

The physics of loosely-bound and halo nuclei is very important in the enhancement of knowledge about the complete nature of strong interactions in general, and nuclear forces in particular. Although such nuclei are widely studied, very little has been said about the effect of the size of the core on the properties of the nucleus. This dissertation investigates if there is correlation between the ground-state energies as well as the root-mean-square radii of the ^{20}C, ^{21}C and ^{22}C halo nuclei. We treat the systems as three-body quantum systems consisting of a core and two valence neutrons and use phenomenological potentials to describe neutron-neutron and core-neutron interactions. We adopted parameters of the potentials that were shown in the literature to correctly describe basic properties of halo nuclei in general. The Faddeev equations for the systems are solved using the hyperspherical harmonics approach. The results suggest that there maybe a direct proportion relationship between the halo nuclear core size and the ground-state energy as well as the root-mean-square radius of the nucleus.

Keywords: Halo nucleus; Faddeev equations; Hyperspherical harmonics; Ground-state energy; Nuclear Potential; Root-mean-square radius; Three-body systems

Contents

List of Tables

List of Figures

Chapter 1

Introduction

Atomic nuclei are composed of positively charged protons and neutral neutrons (nucleons). There is a limit on the allowed maximum number of nucleons that a nucleus can have to exist. This limit is shown with lines, called drip lines, marked with $B_p = 0$ and $B_n = 0$ energy units, respectively, for protons and for neutrons in Figure 1.1, where B represent binding energy. The figure displays a two-dimensional chart of known nuclei as a function of the number of proton (Z) and the number of neutrons (N). A nucleus is said to be stable if it has a long half-life [1], otherwise it is unstable. Theoretical and experimental studies of properties of nuclei have revealed correlations between the number of nucleons in a nucleus and properties, such as the binding energy and the size, of the nucleus. It has also been established that the nuclear force is strong and of short range in nature [2]. This causes nuclei to be very compact structures with high density. However, there exist nuclei with some weakly bound nucleons forming a cloud (halo) around a compact core [3], see for example Figure 1.2 for an illustration (the figure should not be treated literally). Such nuclei are unstable against absorbsion of additional nucleons and, as will be explained later, do not exhibit properties similar to those of normal nuclei.

The physics of loosely-bound nuclei and halo nuclei is very important in the enhancement of knowledge about the true nature of strong interactions in general, and nuclear forces in particular. Halo nuclei are defined as nuclei that have weakly-bound nucleons orbiting a core. In these nuclei, one or more of the nucleons spend more time beyond the radius of the nuclear potential [3, 4]. As a result, halo nuclei are weakly-bound

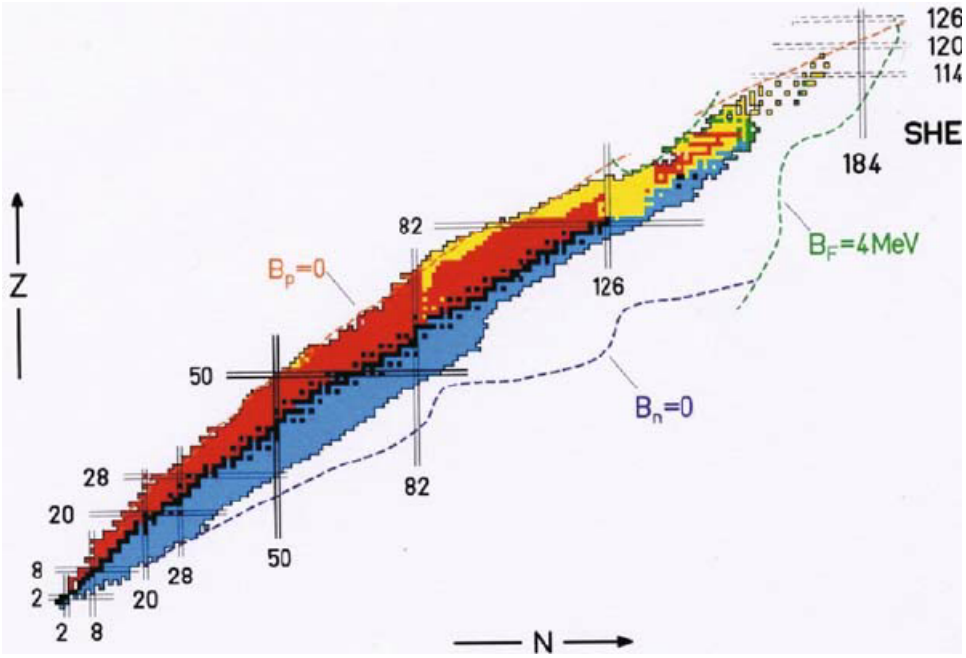

Figure 1.1: A chart of known nuclei showing neutron and proton drip lines, marked with $B_n = 0\,\text{MeV}$ and $B_p = 0\,\text{MeV}$, respectively. Black squares represent stable nuclei and SHE stand for *Super Heavy Elements*. The figure is taken from Ref. [5].

and have a radius comparable to that of a larger normal stable nucleus, as illustrated in Figure 1.2. The discovery of halo nuclei was done by Tanihata *et al.* [6] in mid 1980's while they were measuring the interaction cross section of certain neutron-rich isotopes of helium and lithium, which are close to the being unstable against loosing neutrons. It was found that some of the nuclei such as ^{11}Li, ^{14}Be and ^{17}Be had a larger root-mean-square radius than expected. This was further emphasized by Hansen and Jonson [7] that the neutron halo in the nucleus affect the nuclear structure and nuclear reaction. It is, therefore, useful to study bound-state properties of halo nuclei to further understand their structure and reaction properties.

Despite spectacular progress in the study of loosely-bound systems [3, 4], there remain many questions that still need to be unanswered, such as: the effect of weak binding on

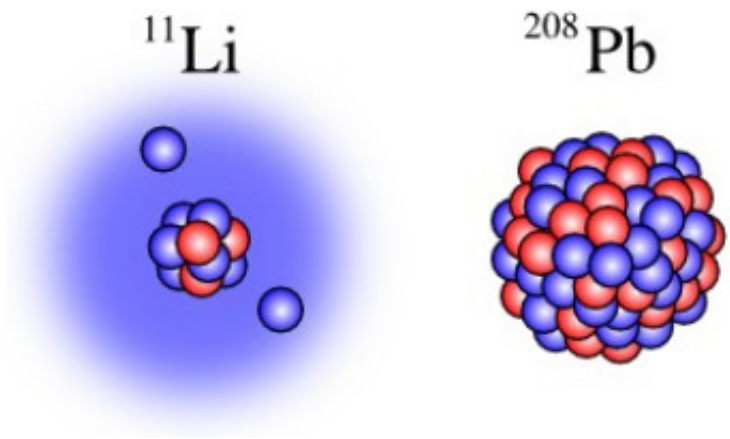

Figure 1.2: Illustration of the halo nuclear size. A halo nucleus (left) and a normal nucleus (right). The figure is taken from Ref. [8].

nuclear structure, nuclear decay, as well as on nuclear reactions, have not yet been fully investigated. In addition, despite many extensive studies of proton halo and neutron halo systems, their structural similarities and differences are yet to be fully clarified. In two-body proton halo and neutron halo systems, the fundamental difference lay in the core-proton Coulomb interaction, which is nonexistent in a neutron-halo system. Therefore, the neutron is expected to be located at a larger distance from its core, compared to the proton. Consequently, the neutron-halo ground-state wave function will exhibit a longer tail in the asymptotic region, compare to the proton-halo ground-state wave function. Another consequence of the lack of a core-neutron Coulomb barrier, is that considering the neutron-rich region of the nuclear chart, as the neutron separation energy approaches zero, the loosely-bound neutron moves far away from the core nucleus, where it possibly couples resonant and unbound continuum states, leading to an unstable quantum system [9, 10, 11, 12, 13, 14]. The physics of such systems, where the binding is dominated by particle interactions instead of the mean field effects, is still wholly unclear. The Coulomb barrier in the core-proton would possibly prevent the occurrence of a halo nucleus that is unstable against proton loss. If this can be proven, it can stand as one of the main differences in two-body proton-halo and neutron-halo

systems.

The many studies of halo nuclei have revealed that these nuclear systems have binding energies that are lower than the excitation energies of the core and have root-mean-square radii that are larger than the size of the core [15]. The separation energies of halo nucleons are much less than in normal nuclei. In addition, the halo nucleons occupy states with lower orbital angular momentum and contribute the most to the ground states of these systems. Although such nuclei are widely studied, very little has been said about the effect of the size of the core on the structure or properties of the halo nucleus. Studies of correlational properties in halo nuclei may be significant to the discussions of universal properties of halo nuclei [15, 16, 17]. The aim of this dissertation is to investigate the effect of the halo nuclear core size on the ground-state energy and root-mean-square radius of the nucleus. For this purpose, we consider carbon isotopes where the nuclear core size varies by one nucleon.

There is continued interest in the existence and structure of neutron-rich Carbon isotopes [3, 4, 6, 17]. Earlier studies [18, 19] suggested that there is a possibility of the existence of the ^{21}C isotope. However, it has now been established [20, 21, 22] that the ^{21}C is unbound, and the search for this system still continue. The interest in ^{21}C is generated by the level structure of the ^{22}C isotope which is a Borromean two-neutron halo nucleus [23]. It is believed [23, 24] that the understanding of the ^{21}C isotope may explain some of the properties of the ^{22}C isotope. In this dissertation we constrain the ^{21}C system to a bound two-neutron halo system. We then compare the ground-state energy and root-mean-square radius of the system with those of the adjacent ^{20}C and ^{22}C isotopes. Here the systems are treated as three-body systems consisting of an inert core and two valence neutrons. The core size in the three systems differ by one unit of mass. Phenomenological potentials are adopted to describe neutron-neutron and core-neutron interactions in the systems.

Halo nuclei are quantum mechanical systems which are accurately described by the many-body Schrödinger equation. Theoretical studies of such systems require the solution of this equation to extract properties such as energy levels, root-mean-square radii and binding energies of the systems [25]. However, it is difficult to solve the many-body Schrödinger equation, even numerically because of the many degrees-of-freedom that need to be considered. Generally, simplifying techniques to reduced complicity of the many body equation are employed to render the equation tractable for numerical solution. A practical and traditional technique, adopted in this work, is to use the cluster method where the many-body system is reduced to a few-cluster system that can then be treated with few-body methods, which are proven exact and accurate. The more common and efficient few-body methods in this regard are the Faddeev method [26, 27, 28, 29, 30, 31, 32, 33] and the Hyperspherical harmonics expansion (HHE) [34, 35, 37, 38, 39, 40]. These methods have been extensively and successfully utilised in studies of a variety of few-atomic, nuclear and particle systems. Both these methods, though they generate solutions, that reproduce known properties of systems, have some limitations. For example, Faddeev method is fully implementable only in three-body and four-body systems. The HHE method, on the other hand, leads to an infinite number of coupled ordinary differential equations related to the partial waves of the system. However, for weakly interacting systems only a few of the HHE equations need to be considered. In this dissertation these two few-body methods are combined to construct solutions to the halo nuclear systems.

The Faddeev method entails decomposing the many-body Schrödinger wave function into a sum of two-body amplitudes. The integrodifferential equations obeyed by these amplitudes are equivalent to the original Schrödinger equation. The Faddeev equations have been applied in studies of bound and scattering processes in three-body nuclear systems [28, 29], were converged results were obtained. The Hyperspherical harmonics

expansion was first introduced in 1937 [41], by Delves when describing the three-body channels in atomic, nuclear reactions and particle physics. The method was used to solve the many-body Schrödinger equation by expressing the equation in hyperspherical coordinates. In these hyperspherical coordinates, the many-body Schrödinger wave function for the system is expanded in an infinite series of partial hyperwaves. The Schrödinger equation then transforms into a set of infinite coupled differential equations. This approach has been used to study several quantum mechanical systems of bound state and scattering problems [34, 35], were converged results were obtained. Our problem of interest involve weakly bound three body systems. Such system are accurately described by very few hyperspherical harmonics [36]. We use this method to construct bound-state solutions of the Faddeev amplitudes to extract properties of two-nucleon halo nuclei. This approach is implemented in the code FaCE [42] that efficiently solves the three-body Faddeev equations.

This dissertation is structured as follows. In Chapter 2, we introduce hyperspherical coordinates required to describe three-body systems. We summarise the features of the Schrödinger equation in hyperspherical coordinates and define hyperspherical harmonics. We conclude the chapter by presenting the Faddeev equations for three-body systems and highlight their association with the original Schrödinger equation. In Chapter 3, we present and discuss convergence results for the ground-state energies and root-mean-square radii of three two-neutron Carbon halo nuclei. We make concluding remarks in Chapter 4 based on the converged results of our study.

Chapter 2

Three-Body Systems

We study three-body systems consisting of two neutrons and a core. To extract internal properties of the systems, we need to eliminate contributions of the center-of-mass kinetic energy of the systems. This is achieved by describing the systems in Jacobi coordinates, which are then used to construct the corresponding hyper spherical coordinates. The discussion of these coordinate systems is now commonplace.

2.1 Jacobi coordinates

Consider a system of three particles, each of mass m_i and position vector $\boldsymbol{r}_i$ $(i = 1, 2, 3)$. There are three different Jacobi relative vectors for this system when all the particles are non-identical. One set of Jacobi vectors for the system is defined by [43]

$$\boldsymbol{x}_i = \left[\frac{m_j m_k}{m_j + m_k}\right]^{1/2} (\boldsymbol{r}_j - \boldsymbol{r}_k) \tag{2.1}$$

$$\boldsymbol{y}_i = \left[\frac{m_i(m_j + m_k)}{M}\right]^{1/2} \left(\boldsymbol{r}_i - \frac{m_j \boldsymbol{r}_j + m_k \boldsymbol{r}_k}{m_j + m_k}\right) \tag{2.2}$$

$$\boldsymbol{R}_{cm} = \frac{1}{M} \left(m_i \boldsymbol{r}_i + m_j \boldsymbol{r}_j + m_k \boldsymbol{r}_k\right\} \tag{2.3}$$

where $\boldsymbol{R}_{cm}$ is the center-of-mass and $M = m_i + m_j + m_k$ the total mass of the system. The mass-dependent coefficients in (2.1) and (2.2) define the reduced masses

$$\frac{1}{\mu_{jk}} = \frac{1}{m_j} + \frac{1}{m_k} \qquad \text{and} \qquad \frac{1}{\mu_{jk,i}} = \frac{1}{m_i} + \frac{1}{m_j + m_k}$$

of the two-body and three-body subsystems, respectively, The other two sets of Jacobi vectors are constructed through the rotation

$$\begin{bmatrix} x_k \\ y_k \end{bmatrix} = \begin{bmatrix} \cos\nu_{ki} & \sin\nu_{ki} \\ -\sin\nu_{ki} & \cos\nu_{ki} \end{bmatrix} \begin{bmatrix} x_i \\ y_i \end{bmatrix} \tag{2.4}$$

where ν_{ki} is defined by $\tan\nu_{ki} = -\sqrt{m_j\, M/(m_i\, m_k)}$. The three sets of Jacobi coordinates are illustrated in Figure 2.1.

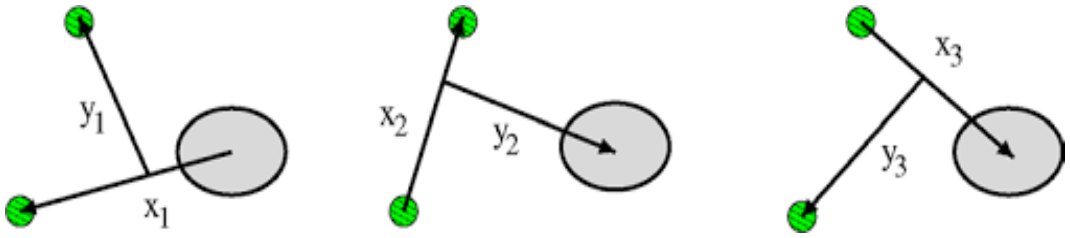

Figure 2.1: Illustration of Jacobi coordinates for a three-body system [44].

The quantum mechanical description of this system is in the form of a Hamiltonian, the eigenfunctions of which are used to determine properties of the system. The Hamiltonian has the form

$$H = \sum_{i=1} \hat{T}_i + \sum_{p,i<j} V_{ij}^p(\boldsymbol{r}_j - \boldsymbol{r}_i)\, \hat{\mathcal{O}}_{ij}^p \tag{2.5}$$

where $\hat{T}_i$ represent the kinetic energy operator of particle i and V_{ij}^p the interaction potential of between particles, i and j. The operators $\hat{\mathcal{O}}_{ij}^p$ depend on other degrees-of-freedom of the particles, such as momentum, energy, spin and isospin. The dominant components of nuclear interaction potentials are [45]

$$\hat{\mathcal{O}}_{ij}^1 = I \ : \text{ central operator} \tag{2.6}$$

$$\hat{\mathcal{O}}_{ij}^2 = \boldsymbol{\ell}_{ij} \cdot \boldsymbol{s}_{ij} \ : \text{ spin-orbit operator} \tag{2.7}$$

$$\hat{\mathcal{O}}_{ij}^3 = S_{ij} \ : \text{ tensor operator} \tag{2.8}$$

where I is a unit matrix and $\boldsymbol{\ell}_{ij}$ the relative orbital angular momentum between the interacting particles. With $V^p(\boldsymbol{r}_{ij})$ as the corresponding form factors. The potential form factors $V^p(\boldsymbol{r}_{ij})$ are a mathematical representation of how the particles interact as a function of their separation distance. Only two-body interactions are considered in these systems because they are more dominant in nuclear systems [46].

Since we are interested in the internal properties of the system, we must eliminate the center-of-mass kinetic energy contribution from (2.5). In Jacobi coordinates, the Hamiltonian (2.5) transforms to

$$H = \hat{T}_{cm} + \hat{T} + \sum_{p,i<j} V_{ij}^p \left(\frac{x_k}{\sqrt{\mu_{ij}}} \right) \hat{\mathcal{O}}_{ij}^p \tag{2.9}$$

where μ_{ij} is the reduced mass of the interacting particles (ij), $\hat{T}_{cm}$ and $\hat{T}$ represent the center-of-mass and internal kinetic energy operators of the system, respectively. This Hamiltonian, without $\hat{T}_{cm}$, is used to construct the wave functions and energy spectra for the system.

2.2 The hyperspherical harmonics

The hyperspherical coordinates (ρ, Ω) for the three-body system consist of the hyperradius ρ, the hyperangles ϕ_i, and a set of spherical polar angles for the vectors $\boldsymbol{x}(x, \theta_x, \varphi_x)$ and $\boldsymbol{y}(y, \theta_y, \varphi_y)$. This results in a set of five angles $\Omega \equiv \{\phi, \theta_x, \varphi_x, \theta_y, \varphi_y\}$. The hyperradius ρ and the hyperangles ϕ_i for the system are defined from the magnitudes of the Jacobi vectors by

$$\rho = \sqrt{x_i^2 + y_i^2} \tag{2.10}$$

$$\tan \phi_i = \frac{y_i}{x_i} \tag{2.11}$$

where $\rho \in [0, \infty)$ and $\phi_i \in [0, \frac{1}{2}\pi]$. The hyperradius is invariant under the permutations and rotations of the particles in the system, whereas ϕ_i is sensitive to these operations.

The transformations of the two-body interaction potentials to hyperspherical coordinates lead to form factors of the form $V(\rho, \Omega)$. However, the internal kinetic energy operator assumes a more involved form [47]

$$\hat{T} = -\frac{\hbar^2}{2m_N}\left[\frac{\partial^2}{\partial\rho^2} + \frac{5}{\rho}\frac{\partial}{\partial\rho} - \frac{\hat{K}^2(\Omega_i)}{\rho^2}\right] \tag{2.12}$$

where $\hat{K}^2$ is the hyperangular momentum operator of the system. This operator has the form

$$\hat{K}^2(\Omega_i) = -\frac{\partial^2}{\partial\phi_i^2} - 4\cot(2\phi_i)\frac{\partial}{\partial\phi_i} + \frac{\hat{l}^2(x_i)}{cos^2\phi_i} + \frac{\hat{l}^2(y_i)}{sin^2\phi_i} \tag{2.13}$$

where $\hat{l}^2$ are orbital angular momentum operators related to the respective Jacobi vectors.

The eigenfunctions $\mathcal{Y}^{L_i}_{K_i M_L}(\Omega_i)$ of this operator satisfy the eigenvalue equation

$$K_i^2(\Omega_i)\,\mathcal{Y}^{L_i}_{K_i M_L}(\Omega_i) = K_i(K_i+4)\,\mathcal{Y}^{L_i}_{K_i M_L}(\Omega_i)\,, \tag{2.14}$$

where $K_i = 2n_i + \ell_{xi} + \ell_{yi}$ and $n = 0, 1, 2, \ldots$. These functions are called hyperspherical harmonics and the corresponding eigenvalues K_i the hyperangular momentum for the system. Hyperspherical harmonics have the general form

$$\mathcal{Y}^{L_i}_{K_i M_L}(\Omega_i) = {}^{(2)}P^{l_{xi}l_{yi}}_{K_i}(\phi_i)\left[Y_{l_{xi}m_{xi}}(\theta_{xi},\varphi_{xi}) \otimes Y_{l_{yi}m_{yi}}(\theta_{yi},\varphi_{yi})\right]_{LM} \tag{2.15}$$

where $Y_{lm}(\theta,\varphi)$ are spherical harmonics, $[\ldots\otimes\ldots]$ implies angular momentum coupling and $[L, M_L]$ the total orbital angular momentum and its azimuthal projection for the system. Here, we define the hyperspherical functions

$${}^{(2)}P^{l_{xi}l_{yi}}_{K_i}(\phi_i) = N^{l_{xi}l_{yi}}_{K_i}(\cos\phi_i)^{l_{xi}}(\sin\phi_i)^{l_{yi}}P^{l_{yi}+\frac{1}{2},l_{xi}+\frac{1}{2}}_{n_i}(\cos 2\phi_i) \tag{2.16}$$

where $P^{a,b}_n(z)$ are Jacobi polynomials with normalisation

$$N^{l_{xi}l_{yi}}_{K_i} = \left[\frac{2n_i!(K+2)(n_i+l_{xi}+l_{yi}+1)!}{\Gamma(n_i+l_{xi}+\frac{3}{2})\Gamma(n_i+l_{yi}+\frac{3}{2})}\right]^{1/2}. \tag{2.17}$$

States with total angular momentum J are constructed by introducing spin functions Φ^{SM_S} in (2.15). The angular momentum coupling, then, leads to

$$\mathcal{Y}^{JM_J}_{K_i\alpha_i}(\Omega_i) = \left[\, \mathcal{Y}^{L_i}_{K_iM_L}(\Omega_i) \otimes \Phi^{S_iM_S} \,\right]^{JM_J} . \tag{2.18}$$

where $\alpha \equiv \{\, \ell_x, \ell_y, L, S, J, s \,\}$ is a set of angular momentum quantum numbers. The spin functions are constructed by coupling the spins of the particles in the same way as in (2.15) for orbital angular momentum.

Hyperspherical harmonics are widely discussed in the literature and their properties are well known. Here, we only highlight relevant key properties of these functions. The hyperspherical harmonics are orthonormal,

$$\left\langle \mathcal{Y}^{JM_J}_{K_j\alpha_j}(\Omega_j) \,\middle|\, \mathcal{Y}^{JM_J}_{K_i\alpha_i}(\Omega_i) \right\rangle = \delta_{K_iK_j}\, \delta_{\alpha_i\alpha_j} , \tag{2.19}$$

and form a complete set of functions, where $\langle \ldots | \ldots \rangle$ implies integration over all the angles. Therefore, angular part of the wave function for the system can expanded in terms of these functions. The hyperspherical harmonics in one Jacobi partition can be expressed in terms of those in another partition through rotations, permutations and parity operators. For this purpose, the general relation [42]

$$\begin{aligned} \mathcal{Y}^{JM_J}_{K_i\alpha_i}(\Omega_i) \;=\; & \sum_{K_j\alpha_j} C(\alpha_i)\, W(L_i, S_i, J, s_i; J_i, S_T)\, W(s_j, s_k, S_T, s_i; S_i, S_j) \\ & \times W(s_j, S_j, J, L_j; S_T, J_j)\, \langle l_{xi} l_{yi} | l_{xj} l_{yj} \rangle_{K_jL_j}\, \mathcal{Y}^{JM_J}_{K_j\alpha_j}(\Omega_j)\, \delta_{L_iL_j} \end{aligned} \tag{2.20}$$

applies, where $C(\alpha)$ are constants, W angular momentum coupling Wigner coefficients and $\langle l_{xi} l_{yi} | l_{xj} l_{yj} \rangle_{K_jL_j}$ Raynal-Revai rotation coefficients [48]. In the special case of systems of spin 0 bosons, only the coefficients $\langle l_{xi} l_{yi} | l_{xj} l_{yj} \rangle_{K_jL_j}$ are required.

2.3 Faddeev equations

In this section, we present a generalized summary of the formulations of Ref. [42]. We are interested in nuclear states that have definite total angular momentum J. The

Faddeev formalism is based on the decomposition of the Schrödinger wave function Ψ^{JM} of the three-body system into three two-body amplitudes $\psi_i^{JM}(x_i, y_i)$, each depending only on one set of Jacobi coordinates

$$\Psi^{JM} = \psi_1^{JM}(x_1, y_1) + \psi_2^{JM}(x_2, y_2) + \psi_3^{JM}(x_3, y_3)\,. \tag{2.21}$$

The total wave function is equivalent to the solution of the Schrödinger equation for the system. The Faddeev amplitudes satisfy the coupled Faddeev equations

$$\begin{aligned}
\left(T_{x1} + T_{y1} + V_1 - E\right)\psi_1^{JM} &= -V_1\left(\psi_2^{JM} + \psi_3^{JM}\right) \\
\left(T_{x2} + T_{y2} + V_2 - E\right)\psi_2^{JM} &= -V_2\left(\psi_3^{JM} + \psi_1^{JM}\right) \\
\left(T_{x3} + T_{y3} + V_3 - E\right)\psi_3^{JM} &= -V_3\left(\psi_1^{JM} + \psi_2^{JM}\right)
\end{aligned} \tag{2.22}$$

where T_x and T_y are the relative kinetic energy operators along the Jacobi coordinates, $V_i = V_{jk}(r_{jk})$ the two-body interaction potentials and E the energy of the system. When the particles have internal structure, then the internal Hamiltonian of the particles must be added to each equation [42].

The number of equations describing systems that consist of two or three identical particles reduces to two or one, respectively. This is because the amplitudes to be determined are identical in such cases. For example, in the case of two identical particles, equations (2.22) reduce to [42]

$$\begin{bmatrix} T_{xi} + T_{yi} + V_i - E & V_i\left(1 + P_{jk}\right) \\ V_k & T_{xi} + T_{yi} + V_k\left(1 + P_{jk}\right) - E \end{bmatrix} \begin{bmatrix} \psi_i \\ \psi_k \end{bmatrix} = 0 \tag{2.23}$$

where P_{jk} is the spin-dependent permutation operator for particles j and k. Note that two-neutron halo nuclei belong to this category of systems. These equations are then transformed to the hyperspherical coordinates as discussed in the previous section. The internal kinetic energy operator is the same as (2.12) and the interaction potential will assume the form $V(\rho, \Omega)$, as indicated earlier.

Now we construct the solutions of the Faddeev equations in the hyperspherical coordinates described in the previous section. In these coordinates, we introduce a partial wave decomposition of the Faddeev amplitudes and assume a separable form

$$\psi_i^{JM}(\rho,\phi_i) = \rho^{-5/2} \sum_{\alpha_i K_i} U^{i,J}_{\alpha_i K_i}(\rho)\, {}^{(2)}P^{l_{xi} l_{yi}}_{K_i}(\phi_i)\,|\, i:\alpha_i \,\rangle^J \tag{2.24}$$

where $i = 1, 2, 3$ and we use the notation of Ref. [42]. Using orthonormalised bases expansion for the Faddeev amplitudes greatly simplifies the determination of the matrix elements for the Hamiltonian operators in (2.22). Choosing the eigenfunctions of the kinetic energy operator, like the hyperspherical harmonics, allows for the analytical evaluation of the angular component of the kinetic energy operator. Introducing the bases expansion (2.24) to the Faddeev equations (2.22) reduces the equations to a set of coupled equations

$$\left[-\frac{h^2}{2\mu_i}\left(\frac{d^2}{d\rho^2} + \frac{(K_i+\frac{3}{2})(K_i+\frac{5}{2})}{\rho^2}\right) - E\right] U^i_{\alpha_i K_i}(\rho) = - \sum_{j,\alpha_j,K_j} V^{ij}_{\alpha_i K_i,\alpha_j K_j}(\rho)\, U^j_{\alpha_j K_j}(\rho) \tag{2.25}$$

where

$$V^{ij}_{\alpha_i K_i,\alpha_j K_j}(\rho) = \sum_p \left\langle\, {}^{(2)}P^{l_{xj} l_{yj}}_{K_j}(\phi_j)\right| V^p(\rho,\phi_i) \left|\, {}^{(2)}P^{l_{xi} l_{yi}}_{K_i}(\phi_i)\,\right\rangle \langle\, j:\alpha_j \,|\, \hat{O}^p_{ij} \,|\, i:\alpha_i \,\rangle \tag{2.26}$$

is the potential coupling matrix elements. Equations (2.25) are solved with the boundary conditions $U(0) = 0$ and $U(\infty) = 0$.

The evaluation of the potential matrix elements is quite involved and the details can be found in Ref. [42], for example. For convenience, we state the results for the central, spin-orbit and tensor operators. For the central components one obtains $\langle\, j:\alpha_j \,|\, i:$

$\alpha_i\,\rangle = \delta_{ij}\delta_{\alpha_i\alpha_j}$ while for the spin-orbit and tensor operators, one obtains [42]

$$\begin{aligned}\langle i:\alpha_i'\|\, C_Q(\hat{l}_{xi})\cdot C_Q(\hat{s}_i)\,\|i:\alpha_i\rangle &= \delta_{s_j's_j}\delta_{s_k's_k}\delta_{JJ'}\delta_{l_{yi}'l_{yi}}\delta_{S_{xi}'S_{xi}}(-1)^{J'+2J_i+l_{yi}'+L_i'+L_i+K+S_{xi}'}\\ &\times\hat{J}_i'\hat{J}_i\hat{L}_i'\hat{L}_i\hat{l_{xi}'}\hat{l_{xi}}\hat{s}_i\hat{s}_i'\begin{Bmatrix} J_i' & J_i & Q\\ s_i & s_i' & J'\end{Bmatrix}\begin{Bmatrix} J_i' & J_i & Q\\ L_i & L_i' & S_{xi}'\end{Bmatrix}\\ &\times\begin{Bmatrix} L_i' & L_i & Q\\ l_{xi} & l_{xi}' & l_{yi}'\end{Bmatrix}\begin{pmatrix} l_{xi}' & Q & l_{xi}\\ 0 & 0 & 0\end{pmatrix}\begin{pmatrix} s_i' & Q & s_{xi}\\ -K' & 0 & K\end{pmatrix},\end{aligned} \tag{2.27}$$

$$\begin{aligned}\langle i:\alpha_i'\|\, T_2(s_js_k)\cdot C_2(l_{xi})\,\|i:\alpha_i\rangle &= \delta_{s_i's_i}\delta_{s_j's_j}\delta_{s_k's_k}\delta_{JJ'}\delta_{J_i'J_i}\delta_{l_{yi}'l_{yi}}(-1)^{3J_i+l_{yi}-S_{xi}'}\\ &\times\hat{2}\hat{S_{xi}'}\hat{S_{xi}}\hat{L_i'}\hat{L_i}\hat{l_{xi}}\hat{l_{xi}'}\hat{s_j'}\hat{s_k'}\sqrt{s_j(s_j+1)}\sqrt{s_k(s_k+1)}\\ &\times\begin{Bmatrix} S_{xi}' & S_{xi} & 2\\ L_i & L_i' & J_i'\end{Bmatrix}\begin{Bmatrix} L_i' & L_i & 2\\ l_{xi} & l_{xi}' & l_{yi}'\end{Bmatrix}\begin{pmatrix} l_{xi}' & 2 & l_{xi}\\ 0 & 0 & 0\end{pmatrix}\begin{Bmatrix} S_{xi}' & S_{xi} & 2\\ s_j' & s_j & 1\\ s_k' & s_k & 1\end{Bmatrix}\end{aligned} \tag{2.28}$$

where $\hat{x} = 2x+1$. The objects in the brackets are the Wigner 3-j symbols while those in the curly brackets are the Wigner 6-j and 9-j symbols.

We seek to solve the coupled equations (2.25) by converting to a matrix eigenvalue problem. This is realised by expanding $U(\rho)$ in terms of a set of hyper-radial orthonormal basis functions as

$$U^{i,J}_{\alpha_iK_i}(\rho) = \sum_{n=0}^{N_b} a^{i,n,J}_{K_i\alpha_i}\, R_n(\rho) \tag{2.29}$$

where $a^{i,n,J}_{K_i\alpha_i}$ are the expansion coefficients and $R_n(\rho)$ the orthonormal basis functions. We choose the basis functions

$$R_n(\rho) = \left[\frac{\beta^{\sigma+1}\,n!}{(n+5)!}\right]^{1/2}\rho^{\sigma/2}\,L_n^{\sigma}\big(\beta\rho\big)\exp\left(-\tfrac{1}{2}\beta\rho\right), \tag{2.30}$$

where β is a variational parameter, $L_n^{\sigma}(z)$ the Laguerre polynomials and $\sigma = 3N-4$, with $N=3$ here. These functions affords the analytical evaluation of the overlap matrix and the kinetic energy matrix. They also exhibit the required boundary form of the total wave function for bound states. These basis functions are widely used in

solving quantum mechanical equations [38, 49, 50] because of the indicated advantages.

The matrix elements of the kinetic energy operator, evaluated with the hyperradial basis functions, have the analytical form

$$T_{K_i}^{nn'} = -\frac{h^2}{2\mu} \left\langle R_n(\rho) \left| \left[\frac{d^2}{d\rho^2} + \frac{(K_i+\frac{3}{2})(K_i+\frac{5}{2})}{\rho^2} \right] \right| R_{n'}(\rho) \right\rangle \tag{2.31}$$

$$= \frac{h^2}{2\mu} \left[\frac{6 - 3\,\delta_{nn'} + 2\,n_<}{12} + \frac{K_i(K_i+4)}{60} \big(3\,n_> - 2\,n_< + 3 \big) \right] \tag{2.32}$$

where $n_< = min(n, n')$, $n_> = max(n, n')$ and $\langle\, R_n(\rho) \,|\, \ldots \,|\, R_{n'}(\rho) \,\rangle$ implies integration over ρ. The matrix elements for the coupling potential with the basis functions $R_n(\rho)$ cannot be evaluated analytically. Therefore the matrix elements

$$V_{K_i\alpha_i,K_j\alpha_j}^{ij,nn'} = \langle\, R_n(\rho) \,|\, V_{\alpha_i K_i,\alpha_j K_j}^{ij}(\rho) \,|\, R_{n'}(\rho) \,\rangle \tag{2.33}$$

are evaluated numerically using the Guass-Laguerree quadrature. The evaluation of these matrix elements constitute the bulk of the computation time in the construction of the Hamiltonian matrix.

The eigenvalue problem for the system is obtained by introducing (2.32) and (2.33) in the coupled equations (2.25). This leads to the coupled algebraic equations

$$\sum_{j,K_j\alpha_j} \sum_{n'} \left[T_{K_i}^{nn'}\,\delta_{K_iK_j}\,\delta_{\alpha_i\alpha_j} + V_{K_i\alpha_i,K_j\alpha_j}^{ij,nn'} \right] a_{K_j\alpha_j}^{jn'} = E\,a_{K_i\alpha_i}^{i,n} \tag{2.34}$$

for the system. This eigenvalue problem is solved to determine the expansion coefficients $\boldsymbol{a}$ which are used to construct the solutions for bound and resonant states of the system. The FORTRAN code FaCE [42] implements the method outlined above in a very stable and flexible way. The code is freely available from the journal website.

Chapter 3

Results and Discussion

3.1 Interaction potentials

Theoretical description of a nucleus is formulated in terms of some cluster structure and interaction potentials between the clusters. There are two types of subsystems in neutron halo nuclei - the neutron-neutron and the core-neutron subsystems. The choice of the interaction potentials is usually based on the need to reproduce some of the known properties of the halo nucleus. The potential used in this dissertation are those well explained and widely used in the literature.

There are several realistic nucleon-nucleon potential models available to describe neutron-neutron interactions [2]. In this dissertation, we adopt the nucleon-nucleon GPT potential [51]. This potential satisfactorily explains low-energy neutron-neutron scattering phase shifts which are well understood. In addition, the potential has a soft core that allows fast convergence of the numerical solutions. This potential is given by

$$V_{nn}(r) = V_c(r) + V_{\rm so}(r)\,\boldsymbol{\ell}_I \cdot \boldsymbol{s}_{ij} + V_t(r)\,S_{ij}, \tag{3.1}$$

where $V_c(r)$ (with ℓ-dependent parameters), $V_{\rm so}(r)$, and $V_t(r)$ are the form factors for the central, spin-orbit coupling, and tensor components, respectively. The form factors

are defined as a sum of Gaussian-shaped functions

$$V_c(r) = \sum_{i=1}^{3} V_{ci}^{\ell} \exp\left[-\left(\frac{r}{r_{ci}^{\ell}}\right)^2\right] \tag{3.2}$$

$$V_{\rm so}(r) = V_{\rm so} \exp\left[-\left(\frac{r}{r_{\rm so}}\right)^2\right] \tag{3.3}$$

$$V_t(r) = \sum_{i=1}^{3} V_{ti} \exp\left[-\left(\frac{r}{r_{ti}}\right)^2\right], \tag{3.4}$$

where $V_c(r)$ and $V_t(r)$ are partial-wave dependent. The parameters V_{ci}^{ℓ}, r_{ci}^{ℓ}, V_{ti} and r_{ti} are given in Table 3.1 and Table 3.2 whereas $V_{\rm so} = -114.5$ MeV $\cdot$ fm^2 and $r_{\rm so} = 0.9296$ fm is adopted.

Table 3.1: Parameters of the central $V_c(r)$ component of the nucleon-nucleon GPT potential. These parameters are taken from Ref. [51].

ℓ	V_{c1} [MeV]	r_{c1} [fm]	V_{c2} [MeV]	r_{c2} [fm]	V_{c3} [MeV]	r_{c3} [fm]
0,2	560	0.8109	-390.7	1.031	-1.501	3.205
1	9.335	1.184	-1.37	2.099	0.1663	3.193

Table 3.2: Parameters of the tensor $V_t(r)$ component of the nucleon-nucleon GPT potential. These parameters are taken from Ref. [51].

V_{t1} [MeV]	r_{t1} [fm]	V_{t2} [MeV]	r_{t2} [fm]	V_{t3} [MeV]	r_{t3} [fm]
12.24	1.539	-31.64	0.4039	0.8111	3.015

The core-neutron potential is constructed by treating the core as a rotor that generates a deformed Woods-Saxon field in which the halo neutrons move [52]. The potential consists of a central and a spin-orbit components. For core-neutron interactions, we

used the ℓ-dependent potential $V_{cv}(r)$ which has a structure similar to (3.1) but without the tensor component. The potential has the form

$$V_{cv}(r) = -V_0^{\ell} f(r) + V_{\rm so}(\boldsymbol{\ell} \cdot \boldsymbol{s}) \frac{1}{r} \frac{d}{dr} f(r) \tag{3.5}$$

where the form factors are of the Wood-Saxon form,

$$f(r) = \frac{1}{1 + \exp[(r - R_0)/a_0]}, \tag{3.6}$$

with V_0^{ℓ} and $V_{\rm so}$ as the depth of the central and spin-orbit couplings parts, respectively. The different parameters for the potentials are listed in Table 3.3. These parameters depend deformation parameters and electromagnetic transition of the halo neutrons and have been adjusted to reproduce properties of the systems. The depth of the two components are both ℓ-dependent to allow for flexibility.

Table 3.3: Parameters of the core-neutron Woods-Saxon potential. These parameters are taken from Ref. [54].

System	ℓ	V_0 [MeV]	R_0 [fm]	a_0 [fm]	$V_{\rm so}$ [MeV · fm^2]	Ref.
^{18}C+n	0	59.5	2.699	0.60	32.8	[53]
	2	40.50	2.699	0.60	32.8	[53]
^{20}C+n	0	29.8	3.393	0.65	35	[54]
	2	47.8	3.393	0.65	35	[54]

The effective two-body potentials lead to under binding of the three-body halo nuclei. Therefore, in all the three systems, a hypercentral three-body potential is of the form [54]

$$V_3(\rho) = -\frac{V_{3b}}{1 + (\rho/5)^3} \tag{3.7}$$

where $V_{3b} = 1.6\,\text{MeV}$, was included to account for three-body effects which may be significant in the systems [46]. These effects contribute to the binding energy of the

systems. In addition, unphysical states, which results from niglecting the Pauli exclusion principle in two-body subsystems, were suppressed using Pauli-blocking [42].

The dependence of ground state properties of the systems on the maximum hyperangular momentum (K_{max}) was investigated. The ground-state energies, root-mean-square radii and the wave functions were calculated for various values of K_{max}. The code FaCE is provided with a number of model systems, $n-n-^4$ He and $n-n-^4$ Be for example [42], that we used to test the code. We reproduced all the results listed in the test run of the code. The results for our three system are given and discussed in the following sections.

3.2 $^{20}C \rightarrow {}^{18}C + n + n$

The ground-state energy of the system was calculated for K_{max} varying from 1 to 40. The results for $K_{max} = 20$ to $K_{max} = 40$ are shown in Table 3.4. As observed from the table, the ground-state energy decreases from -0.379020 MeV to -0.383434 MeV as K_{max} increases from 20 to 40, and appears to converge. The convergence of the hyperspherical harmonics solution is expected because of its ability to handle any type of interaction potentials. The convergence pattern of E_0 is illustrated in Figure 3.1. As observed from this figure, the convergence of the ground state energy with increasing K_{max} is quite rapid. The ground state energy of ^{20}C converges to -0.3834 MeV at $K_{max} = 40$. This value is close to -0.32 MeV reported in [56] for the system.

The calculated root-mean-square radius at various values of the maximum hyperangular momentum K_{max} of the system is also given in Table 3.4. As can be seen in the table, the root-mean-square radius appears to converge rapidly as K_{max} increases from 20 to 40. The variation of the two observable is displayed in Figure 3.2, where the convergence of the root-mean-square radius with increasing maximum hyperangular

Table 3.4: Variation of the ground-state energy and root-mean-square radius of ^{20}C with K_{max}.

$K_{\max}$	E_0 (MeV)	$\sqrt{\langle r^2 \rangle}$ (fm)
20	-0.379020	3.671
22	-0.381274	3.690
24	-0.382373	3.703
26	-0.382910	3.711
28	-0.383174	3.716
30	-0.383305	3.718
32	-0.383375	3.722
34	-0.383407	3.723
36	-0.383423	3.723
38	-0.383431	3.724
40	-0.383434	3.724
	-0.32 [56]	2.98±0.05 [57]

momentum K_{max} is clearly observed. The converged value of the root-mean-square is 3.724 fm at $K_{max} = 40$. This value is significantly more than 2.98 fm reported in [57]. The difference is likely to be due to the chosen input potential used in this dissertation.

The significance of the partial waves of this system was determined by calculating the wave functions at different values of the hyperangular momentum. In Figure 3.3 we display the partial waves for $K = 0$, $K = 2$, and $K = 4$. As can be seen in this figure, the $K = 0$ contributes the most to the total wave function. That is, the $K = 0$ partial wave is the dominant partial wave. This is consistent with the established properties of halo nuclei. Also, it is observed that the probability densities of the partial waves is highest around 9 fm, which is well beyond the range of the interaction potentials in the system.

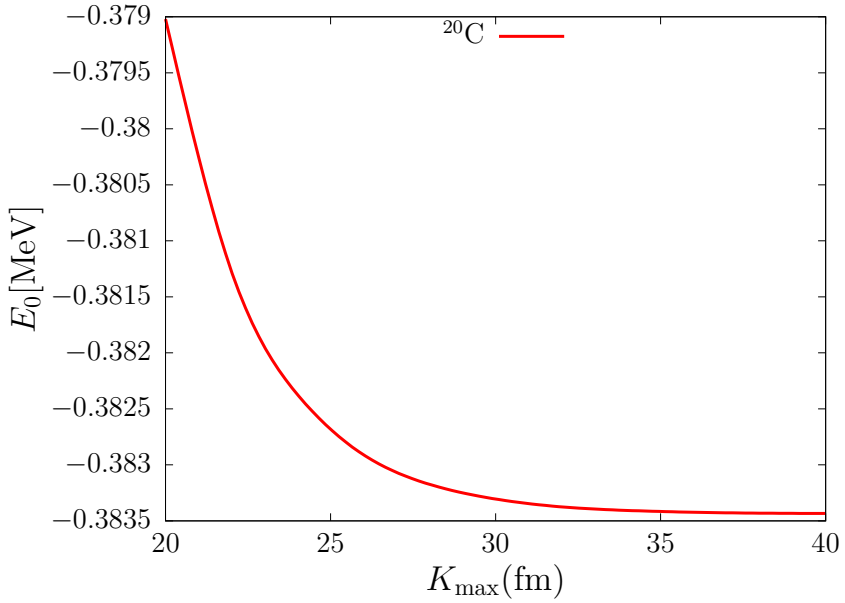

Figure 3.1: Variation of the ground state energy of ^{20}C with increasing maximum hyperangular momentum K_{max}.

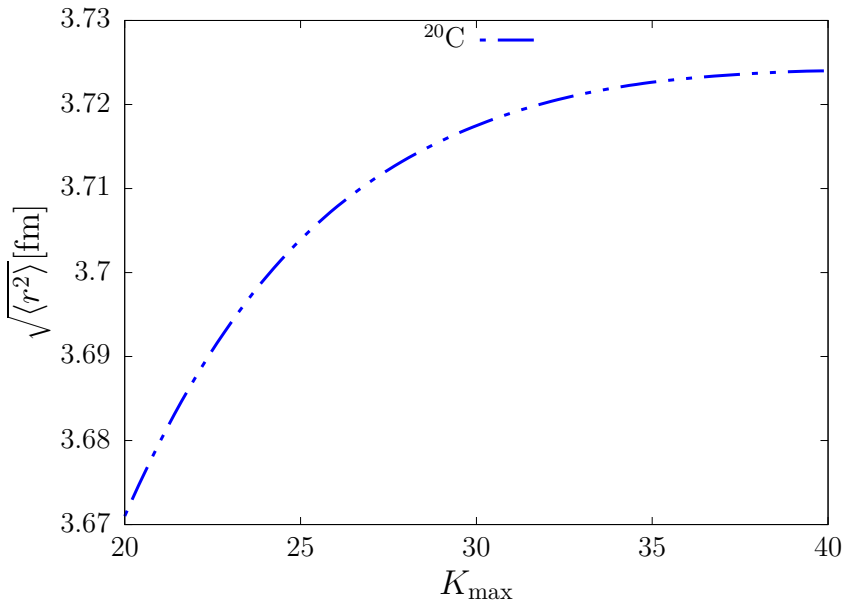

Figure 3.2: Variation of the rms of ^{20}C with increasing maximum hyperangular momentum K_{max}.

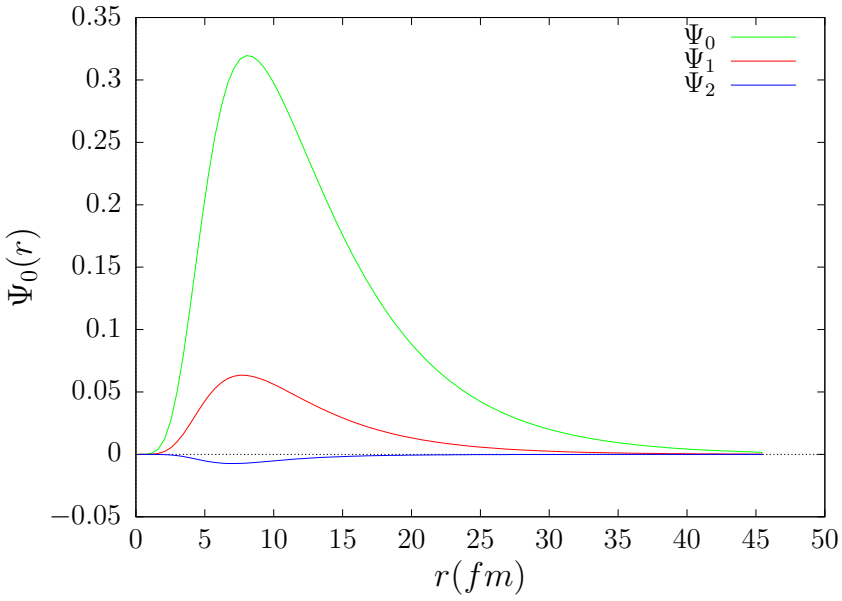

Figure 3.3: Plots of the ^{20}C amplitudes for $K = 0, 2, 4$ as a function of the hyperradius r.

3.3 $^{21}C \rightarrow ^{19}C + n + n$

The ground-state energy of this system was calculated at values of the maximum hyperangular momentum ranging from $K_{max} = 1$ to $K_{max} = 40$. The results are given in Table 3.5 for $K_{max} = 20 - 40$. The calculated ground-state energy converges to -0.4103 MeV as K_{max} increases. This convergence can be readily deduced from Figure 3.4, which shows the variation of the calculated energy with increasing K_{max}. This converged value is significantly lower than the expected value of a resonance ($E_0 > 0$ MeV) recently reported in the literature [21, 22]. However, some studies of carbon isotopes [19, 20] with different potential models also reported $E_0 < 0$ MeV ground-state energy for the system.

The values of the calculated root-mean-square radius of the system are given in Ta-

Table 3.5: Variation of the ground-state energy and root-mean-square radius of ^{21}C with K_{max}.

$K_{\max}$	E_0 (MeV)	$\sqrt{\langle r^2 \rangle}$ (fm)
20	-0.406481	3.628
22	-0.408509	3.645
24	-0.409475	3.655
26	-0.409944	3.662
28	-0.410168	3.666
30	-0.410277	3.668
32	-0.410330	3.669
34	-0.410356	3.670
36	-0.410368	3.671
38	-0.410374	3.671
40	-0.410376	3.671

ble 3.5. The values appear to converge, which is confirmed by the plot of the variation of the root-mean-square radius with K_{max} shown in Figure 3.5. The converged value of the root-mean-square radius is 3.671 fm, which is slightly higher than 3.27 fm [19].

Figure 3.6 shows the partial waves for $K = 0$, $K = 2$, and $K = 4$ for this system. It can be seen in the figure that the $K = 0$ partial wave is the dominant partial wave, as in the case of ^{20}C. Again, the probability densities of the partial waves is highest around 9 fm, which is well beyond the range of the interaction potentials in the system. These observations confirm the halo nature of this system.

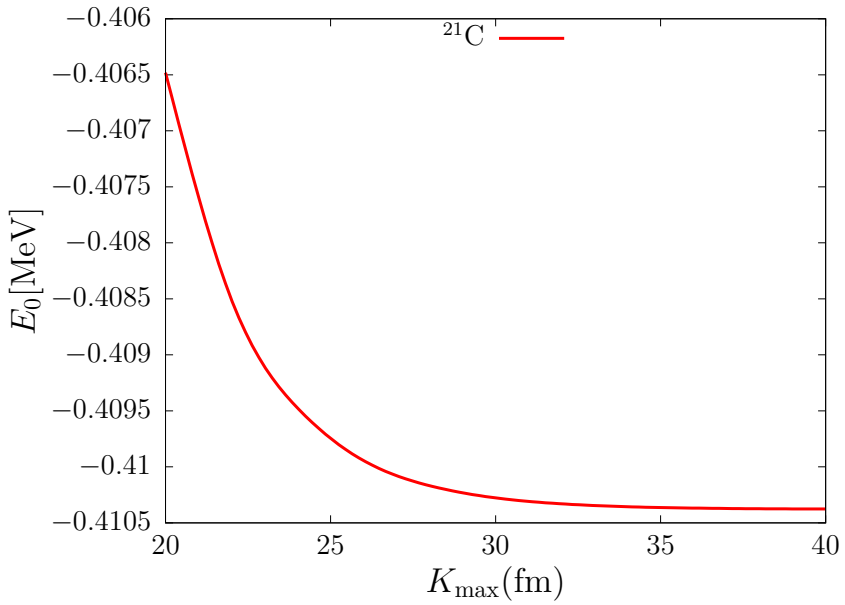

Figure 3.4: Variation of the ground-state energy of ^{21}C with increasing maximum hyperangular momentum K_{max}.

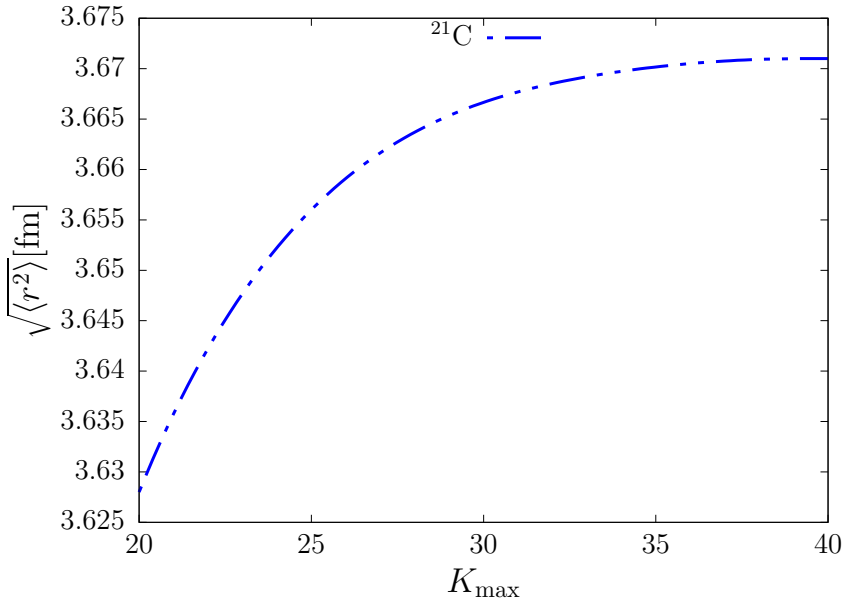

Figure 3.5: Variation of the rms of ^{21}C with increasing maximum hyperangular momentum K_{max}.

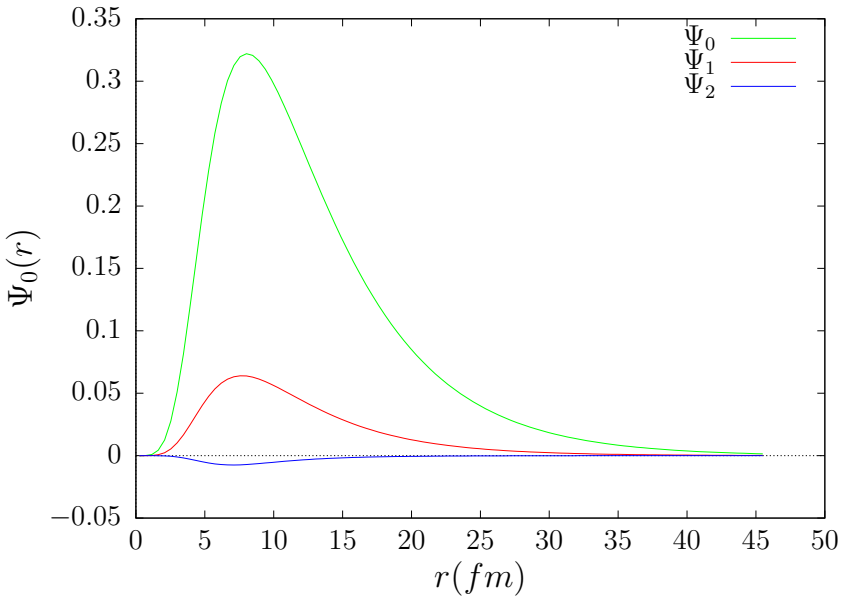

Figure 3.6: Plots of the ^{21}C amplitudes for $K = 0$, 2, 4 as a function of the hyperradius r fm.

3.4 $^{22}C \rightarrow {}^{20}C + n + n$

Table 3.6 shows the calculated ground-state energies of ^{22}C at different values of the maximum hyperangular momentum. As can be noticed from the table, the ground-state energy of the ^{22}C system decreases from -0.431822 MeV to -0.435303 MeV as the hyperangular momentum increases from K_{max}=20 to K_{max}=40. Figure 3.7 clearly shows the convergence of the energy with increase in the maximum hyperangular momentum. The converged value of $E_0 = -0.4353$ MeV compares favourably with the results of $E_0 = -0.4353$ MeV [54] and $E_0 = -0.4353$ MeV [55].

Table 3.6 also presents the calculated values of root-mean-square radii for the system. The convergence of the calculated rms is demonstrated in Figure 3.8. The rms converges from 3.671 fm to 3.724 fm as K_{max} increases from 20 to 40. The converged value of the rms is in excellent agreement with the results $\sqrt{\langle r^2 \rangle} = 3.51$ fm [54] and $\sqrt{\langle r^2 \rangle} = 3.61$ fm [55].

Table 3.6: Variation of the rms of ^{22}C with increasing maximum hyperangular momentum K_{max}.

$K_{\max}$	E_0 (MeV)	$\sqrt{\langle r^2 \rangle}$ (fm)
20	-0.431822	3.590
22	-0.433660	3.603
24	-0.434530	3.613
26	-0.434933	3.618
28	-0.435130	3.621
30	-0.435221	3.624
32	-0.435270	3.625
34	-0.435290	3.626
36	-0.435300	3.626
38	-0.435300	3.626
40	-0.435303	3.626
[55]	-0.442	3.51
[54]	-0.489	3.61

Figure 3.9 shows the amplitudes of the partial waves for $K = 0$, $K = 2$, and $K = 4$ for this system and, again, reveals that the $K = 0$ partial wave is dominant. Also, the probability densities of the partial waves is highest around 9.0 fm, well beyond the range of the interaction potentials in the system. This is consistent with the halo nature of the system.

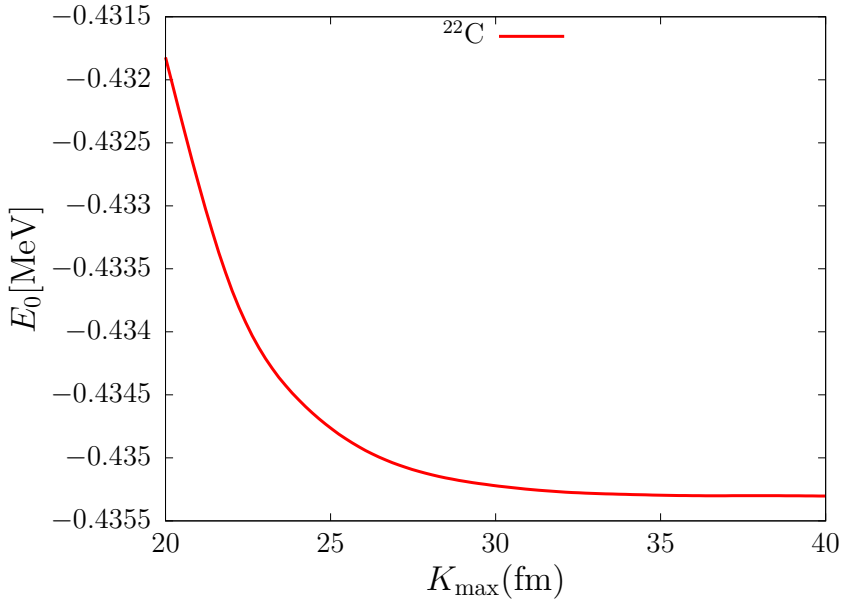

Figure 3.7: Variation of the ground-state energy of ^{22}C with increasing maximum hyperangular momentum K_{max}.

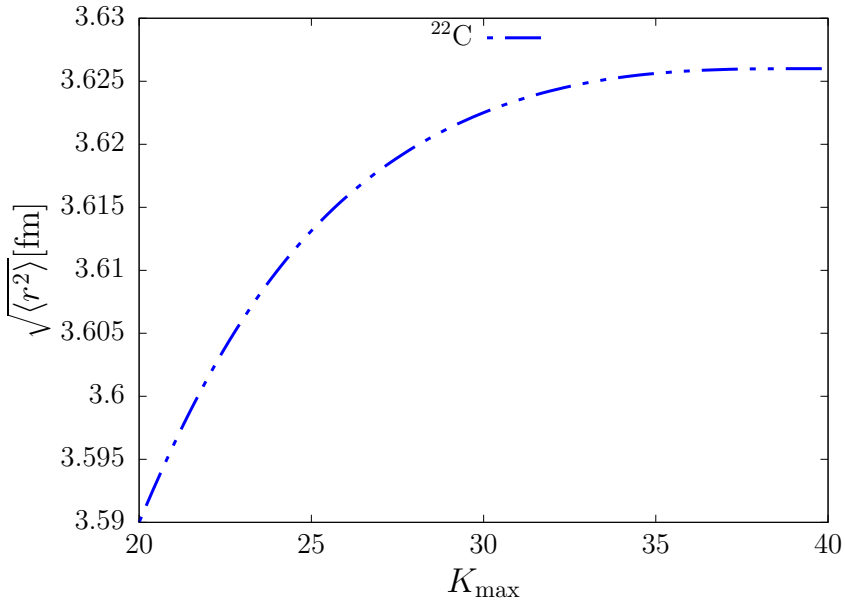

Figure 3.8: Variation of the rms of ^{22}C with increasing maximum hyperangular momentum K_{max}.

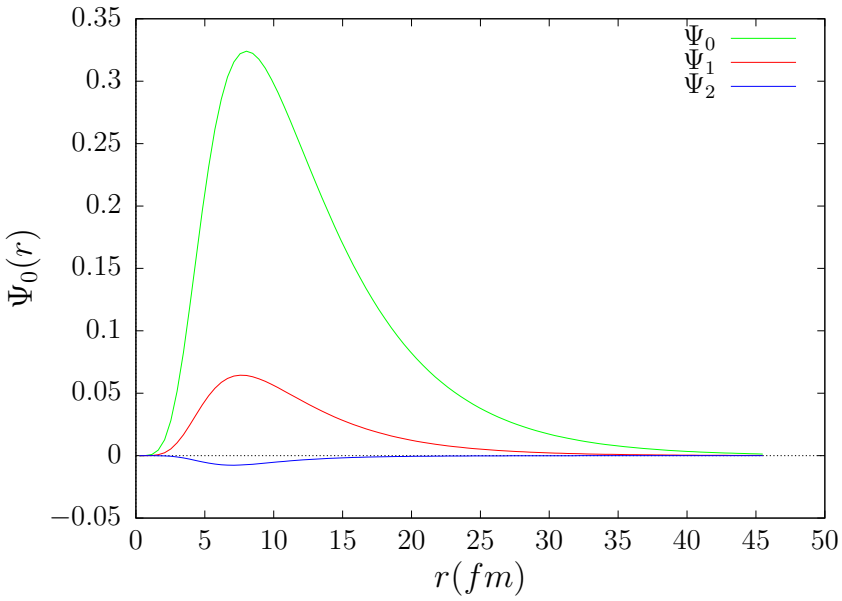

Figure 3.9: Plots of the ^{22}C amplitudes for $K = 0$, 2, 4 as a function of the hyper-radius r fm.

3.5 Remarks on the results

It would be informative to know if there are any correlations among the ground-state properties of the three carbon isotopes. For this reason, we compare the calculate ground-state energies and root-mean-square radii of the systems. The results are summarized in Table 3.7. It can be seen from the table that the ground-state energy of ^{20}C is higher than that of ^{21}C and ^{22}C, while the ground-state energy of ^{22}C is the lowest. We acknowledge that the ground-state energy of the ^{21}C is underestimated in this dissertation. Here we treat this system as bound while is currently known as unbound. Figure 3.10 shows the variation of the ground-state energy of the systems with the atomic number A. It is seen from the figure that the relationship between the two observable is almost linear. A similar, but not so obvious trend was reported in Ref. [19, 20] where the properties of the systems were determined with methods and interaction potentials different from those used in this dissertation. The variation of the root-mean-square radius of the systems with increasing atomic number, given

in Table 3.7 and shown in Figure 3.11, appears to be very small. This observation is surprising because the interaction potential used for the core-neutron is different for each system.

Table 3.7: Ground-state energies and root-mean-square radii for ^{20}C, ^{21}C and ^{22}C at $K_{max} = 40$

System	E_0 (MeV)	$\sqrt{\langle r^2 \rangle}$ (fm)
^{20}C	-0.383434	3.724
^{21}C	-0.410376	3.671
^{22}C	-0.435303	3.626

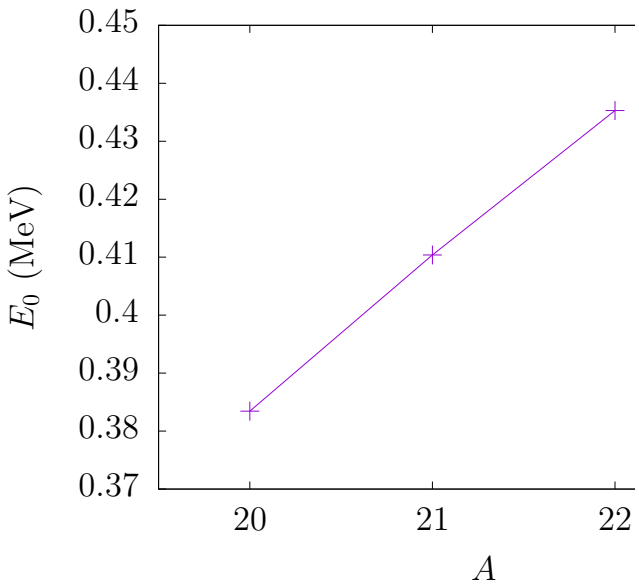

Figure 3.10: The calculated ground-state energy of the carbon isotopes with atomic number A.

In Figure 3.12, we compare the calculated wave functions of the three systems. As can be seen, the waves functions are similar to one another. More specifically, the functions

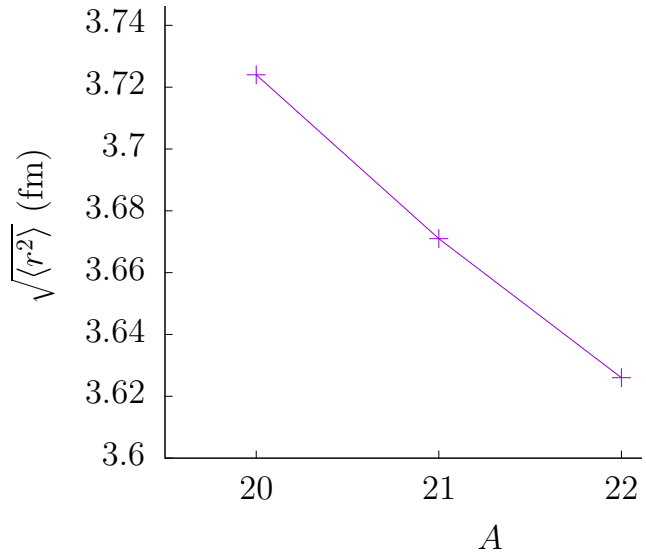

Figure 3.11: Variation of the root-mean-square radii of the carbon isotopes with atomic number A.

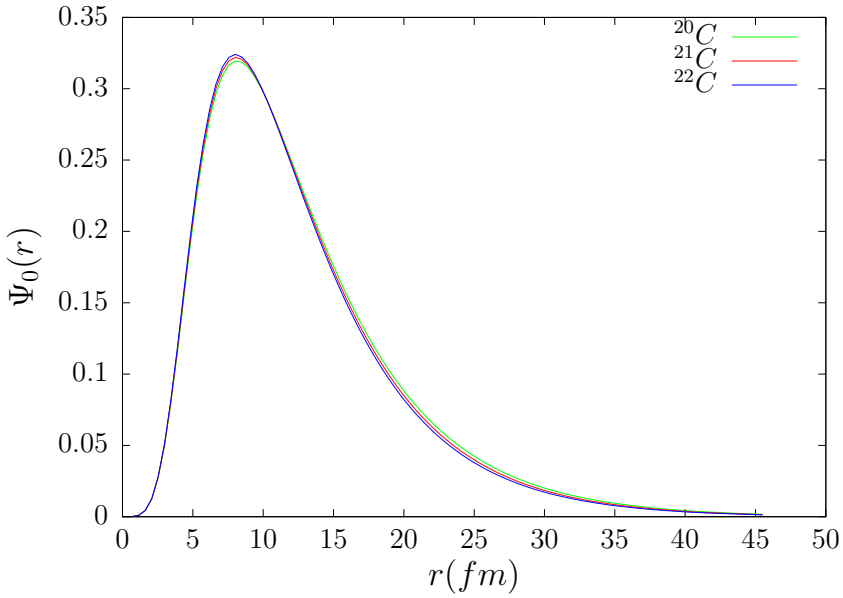

Figure 3.12: Plots of the ^{20}C, ^{21}C and ^{22}C amplitudes for $K = 0$, 2, 4 as a function of the hyperradius r fm.

are identical in the region $r < 8$ fm and slightly different in magnitude for $r > 8$ fm. However, the differences are not significant. This is not surprising because, although

the interaction potentials used are different, they lead to slightly different ground-state energies and almost the same root-mean-square radii for the systems. It is possible that these similarities emanate from the potentials used. That is, the similarities may disappear when a different set of potentials are used to describe the interactions in the systems. This will require further and broader investigations into the effects of input interaction potentials and cluster structure on the properties of these systems.

Chapter 4

Concluding Remarks

In this dissertation, we studied the ground-state properties of the the ^{20}C, ^{21}C and ^{22}C systems. We described the isotopes as three-body systems consisting of an inert core and two neutrons interacting through two-body potentials commonly used in the literature. We solved the three-body Faddeev equations in the hyperspherical harmonics approach to calculate the ground-state energies, root-mean-square radii and the wave functions of the three systems. In the calculations, we kept the parameter space constant while increasing the total hyperangular momentum K_{max}. The convergence patterns of these properties was investigated. We observed that convergence was attained for the ground-state energies and root-mean-square radii at K_{max} in the three systems.

We observed that the ground-state energies of the three systems were generally low which indicates that the systems are weakly bound. This observation is consistent with what is reported in the literature. The energies appeared to decrease with the increase in the atomic number. The root-mean-square radii of systems were almost equal and generally large for systems of this atomic number. This characteristic is also agreement with those reported in the literature. The radii also appeared to decrease, though slightly, with the increase in the atomic number. The wave functions of the systems were also investigated. We observed that the amplitudes of the lowest hyperangular momenta were dominant and contributed the most to the total wave function. This is agreement with observations reported in the literature. The wave functions of the three

systems as a function of the hyperradius r were almost identical with slight differences showing in the region $r > 8$ fm. The probability densities were highest around $r = 9$ fm. All these observations support the identification of the three systems as halo nuclei.

We then investigated the possibility of correlations between the size of the core in the systems and the calculated ground-state properties. Since the systems were all modeled as two-neutron three-body systems, their structural differences could be reduced to the core-size in the systems. We plotted the ground-state energies as a function of the atomic number. The plot showed an almost linear relation between the quantities, which is slightly different from observations reported in the literature. This is because in our modeling, we treated the ^{21}C as bound when it is currently known to be unbound. Adopting this cluster structure was adopted because of earlier experimental reports of a bound ^{21}C system as indicated in Chapter 1. The resulting bound state for this system is, therefore, too deep. We also plotted the root-mean-square radii of the systems as a function of the atomic number and the plot showed an almost linear relation between the quantities. These correlations could simply be as a result of the modeling of the ^{21}C isotope or the interaction potential used. Therefore the this dissertation should be interpreted with caution. This requires further and broader investigation.

Bibliography

[1] S. S. Wong, *Introduction to Nuclear Physics* (2nd Eddition), (New York: Wiley) (1998).

[2] B. V. Danilin, I. J. Thompson, J. S. Vaagen, M. V. Zhukov, Nucl. Phys. A **632**, 383 (1998).

[3] I. Tanihata, H. Savajols and R. Kanungo, Prog. Part. Nucl. Phys. **68**, 21 (2013).

[4] A. S. Jensen, K. Riisager, D. V. Fedorov and E. Garrido, Rev. Mod. Phys. **76** 215 (2004).

[5] B. Rubio, W. Gelletly, Lecture Notes in Physics **764**, 99 (2008).

[6] I. Tanihata, H. Hamagaki, O. Hashimoto, Y. Shida, N. Yoshikawa, K. Sugimoto, O. Yamakawa, T. Kobayashi, and N. Takahashi, Phys. Rev. Lett. **55**, 2676 (1985).

[7] P. G. Hansen and B. Jonson, Europhysics Letters **4**, 409 (1987).

[8] http://www.triumf.ca/galleries/image/halo-nucleus, Retrieved 22 March (2016).

[9] K. Möhring, U. Smilansky, Nucl. Phys. A **338**, 227 (1980).

[10] H. P. Breuer, F. Petruccione, The Theory of Open Quantum Systems, Oxford University Press, 2002.

[11] J. Okolowicz, M. Ploszajczak, I. Rotter, Phys. Rep. **374**, 271 (2003).

[12] J. Dobaczewski, N. Michel, W. Nazarewicz, M. Ploszajczak, and J. Rotureau, Prog. Part. Nucl. Phys. **59** 432 (2007).

[13] U. Weiss, Quantum Dissipative Systems, World Scientific, (2008).

[14] N. Michel, W. Nazarewicz, J. Okolowicz, M. Ploszajczak, J. Phys. G: Nucl. Part. Phys. **37**, 064042 (2010).

[15] D. L. Canham, H. -W. Hammer, Eur. Phys. J. A **37**, 367 (2008).

[16] T. Frederico, A. Delfino, L. Tomio, M.T. Yamashita, Prog. Part. Nucl. Phys. **67**, 939 (2012).

[17] S. Watanabe, K. Minomo, M. Shimada, S. Tagami, M. Kimura, M. Takechi, M. Fukuda, D. Nishimura, T. Suzuki, T. Matsumoto, Y. R. Shimizu, and M. Yahiro, Phys. Rev. C **89**, 044610 (2014).

[18] J. D. Stevenson, P. B. Price, Phys. Rev. C **24** (1981) 2102.

[19] Zhongzhou Ren, Z. Y. Zhu, Y. H. Cai, Gongou Xu, Nucl. Phys. A **605** 75 (1996).

[20] Xiang-Xiang Sun, Jie Zhao, Shan-Gui Zhou, Nucl. Phys. A **1003**, 122011 (2020).

[21] S. Mosby, et al, Nucl. Phys. A **909**, 69 (2013).

[22] Y. Togano, et al, Phys. Lett. B **761**, 412 (2016).

[23] L. Tomio, A. Delfino, T. Frederico, M. R. Hadizadeh, M. T. Yamashita, R. S. Marques de Carvalho, Int. J. Mod. Phys. E **20**, Supp. 1, 254 (2011).

[24] T. Fukui, K. Ogata, EPJ Web of Conferences **66**, 03031 (2014).

[25] T. K. Das and R. Chattopadhyay, Fizika B **2**, 262502 (1993).

[26] C. D. Lin, Physics Reports **257**, 1 (1995).

[27] M. Fontannaz, Nuovo Cimento B **53**, 53 (1968).

[28] G. F. Drukarev, S. A. Pozdneev, Sov. Phys. JETP **47**, 1045 (1978).

[29] S. P. Merkuriev, Ann. Phys. (NY) **130**, 395 (1980).

[30] J. W. Evans, D. K. Hoffman, J. Math. Phys. **22**, 2858 (1981).

[31] S. P. Merkuriev, L. D. Faddeev, Quantum Scattering Theory for Few-Body Systems. Moscow: Nauka 1985 (in Russian).

[32] A. A. Kvitsinsky, A. Wu, C. -Y. Hu, J. Phys. B: At. Mol. Opt. Phys. **28**, 275 (1995).

[33] P. A. Belov, S. L. Yakovlev, Bulletin of the Russian Academy of Sciences. Physics **76**, 913 (2012).

[34] R. Krivec, Few-Body Systems **25**, 199238 (1998).

[35] M Fabre de la Ripelle, Annals of Physics **147**. 281 (1983).

[36] M. Gattobigio, A. Kievsky, M. Viviani Few-Body Syst **54**, 657 (2013).

[37] Md Abdul Khan, T. K. Das, Pramana **57**, 701 (2001).

[38] M. Gattobigio, A. Kievsky, and M. Viviani, Phys. Rev. C **83**, 024001 (2011).

[39] A. Gnech, M. Viviani, and L. E. Marcucci, Phys. Rev. C **102**, 014001

[40] L. E. Marcucci, J. Dohet-Eraly, L. Girlanda, A. Gnech, A. Kievsky, M. Viviani, Front. Phys. **8**, 69 (2020).

[41] T. H. Gronwall, Phys. Rev. **51**, 655 (1937).

[42] I. J. Thompson, F. M. Nunes, B. V. Danilin, Comp. Phys. Commun. **161**, 87 (2004).

[43] V. V. Gusev, V. I. Puzynin, V. V. Kostrykin, A. A. Kvitsinsky, S. P. Merkuriev, and L. I. Ponomarev, Few-Body Syst., **9**, 137 (1990).

[44] F. M. Nunes, Nucl. Phys. A **757**, 349 (2005).

[45] R. B. Wiringa, V. G. J. Stoks, R. Schiavilla, Phys. Rev. C **51**, 38 (1995).

[46] L. E. Marcucci, J. Dohet-Eraly, L. Girlanda, A. Gnech, A. Kievsky, M. Viviani, Front. Phys. **8**, 69 (2020).

[47] P. Descouvemont, C. Daniel, D. Baye : Phys. Rev. C **67**, 044309 (2003).

[48] J. Raynal, J. Revai, Nuovo Cimento **68**, 612 (1970).

[49] G. Erens, J. L. Visschers, R. van Wageningen, Ann. Phys. **67**, 461 (1971).

[50] N. Barnea, W. Leidemann, G. Orlandini, Nucl. Phys. A **650**, 427 (1999).

[51] D. Gogny, P. Pires, and R. De Tourreil, Phys. Lett. B **32**, 591 (1970).

[52] I. Brida, A microscopic hyperspherical model of two-neutronhalo nuclei, PhD tesis (Michigan State University) (2009).

[53] P. Capel, D. Baye and M. S. Mekezhik Phys. Rev. C **68**, 014612 (2003).

[54] Y. Kucuk, J. A. Tostevin, Phys. Rev. C **89**, 034607 (2014).

[55] W. Horiuchi and Y. Suzuki, Phys. Rev. C **74**, 034311 (2006).

[56] N. Kobayashi, T. Nakamura, J. A. Tostevin, Phys. Rev. **C 86**, 054604 (2012)

[57] A. Ozawa, O. Bochkarev, L. Chulkov, D. Cortina, H. Geissel, M. Hellstrm, M. Ivanov, R. Janik, K. Kimura, T. Kobayashi, A. Korsheninnikov, G. Mnzenberg, F. Nickel, Y. Ogawa, A. Ogloblin, M. Pftzner, V. Pribora, H. Simon, B. Sitr, P. Strmen, K. Smmerer, T. Suzuki, I. Tanihata, M. Winkler, and K. Yoshida, Nucl. Phys. **A 691**, 599 (2001).

[58] Y. Togano, T. Nakamura, Y. kondo, J.A Tostevin, A.T Saito et al Phys. Lett. **B 761**, 412-418 (2016)